Reconciling Work Functions and Adsorption Enthalpies for Implicit Solvent: A Pt (111)/Water Interface Case Study

Gabriel Bramley[1], Manh-Thuong Nguyen[2], Vassiliki-Alexandra Glezakou[2], Roger Rousseau[2*], Chris-Kriton Skylaris[1*]*

[1] School of Chemistry, University of Southampton, Southampton SO17 1BJ, UK

[2] Physical Sciences Division, Pacific Northern National Laboratory, Richland, WA 99352, USA

KEYWORDS: continuum solvation, metal/water interfaces, ab initio molecular dynamics, phenol adsorption

ABSTRACT

Implicit solvent models are a computationally efficient method of representing solid/liquid interfaces prevalent in electrocatalysis, energy storage and materials science. However, electronic structure changes induced at the metallic surface by the dielectric continuum are not fully understood. To address this, we perform DFT calculations for the Pt(111)/water interface, in order to compare Poisson-Boltzmann continuum solvation methods with *ab initio* molecular dynamics (AIMD) simulations of explicit solvent. We show that the implicit solvent cavity can be

parametrized in terms of the electric dipole moment change at the equilibrated explicit Pt/water interface to obtain the potential of zero charge (PZC). We also compare the accuracy of aqueous enthalpies of adsorption of phenol on Pt(111) using geometry and charge density based dielectric cavitation methods. The ability to parametrize the cavity according to individual atoms, as afforded in the geometry based approach, is key to obtaining accurate enthalpy changes of adsorption under aqueous conditions. We also show that the electronic structure changes induced by explicit solvent and our proposed implicit solvent parametrization scheme yield comparable density difference profiles and d-band projected density of states. We therefore demonstrate the capability of implicit solvent approaches to capture both the energetics of adsorption processes and the main electronic effects of aqueous solvent on the metallic surface. This work therefore provides a scheme for computationally efficient simulations of interfacial processes for applications in areas such as heterogeneous catalysis and electrochemistry.

1 Introduction

The study of metallic surfaces has garnered significant interest in the modern chemistry and materials communities. Platinum catalysts have received especially close attention given their important role in many emergent technologies such as the conversion of crude bio-oils to transport fuels[1-2] and proton-exchange membrane fuel cells (PEMFCs).[3] In addition to empirical studies, computational simulations of these systems can provide insight into the mechanisms and properties underpinning these processes, guiding design improvements which increase both yields and turn-over frequencies.[4] However, reactivity and selectivity in these applications are strongly influenced by the solvent environment,[5-7] whether through site-blocking at the catalytic surface,[8] stabilization of polar transition states or the introduction of side processes involving the solvent.[9] Given these complex effects, one can find numerous examples where the solvent (usually aqueous) environment can either hinder or aid chemical/industrial processes. For example, the rate of hydrodeoxygenation of ketones on MoO_3 catalysts markedly decreases at high H_2O concentrations.[8] In contrast, aqueous solvent activates the oxidation reaction of ethanol on Au nanoparticles, where the initial O_2 dissociation step is both more thermodynamically favored by increases in the binding energy of Au-O, and kinetically favored through a reduction of the activation energy.[10] Therefore, computationally efficient techniques must be designed to capture the complex phenomena of solvation at the solvent/metal interface, in order to accurately measure the energetics of adsorption which underlie heterogeneous catalytic processes.

One well-known effect of the aqueous environment on metallic surfaces is the reduction of the work function,[11] which increases the reductive strength of heterogeneous catalysts.[12-13] Using DFT simulations of the water mono/multilayer at the Pt(111) surface, Tripkovic et al.[14] showed that the solvent induced work function changes can be decomposed into polarization and orientation

contributions, as defined in the potential of zero charge (PZC) model of Trassati.[15] The orientation contribution is the work function change produced by the net dipole moment of molecular water, while the polarization contribution corresponds to the electric dipole moment induced by charge transfer/Pauli repulsion[16] effects at the metallic/water interface. However, static configurations fail to represent the dynamic nature of water. In reality, the rotational freedom of solvent causes the overall dipole moment to evolve over time, meaning no single water structure can represent the work function. Although the experimental potential of zero charge is measured as a macroscopic average over a large system, computed values across small simulation cells require an ensemble average of the work function from multiple configurations. Sakong et al.[17-18] performed *ab initio* molecular dynamics (AIMD) simulations of the water/Pt(111) interface, showing that the mean work function decreases to 5.0 eV compared to the vacuum value of 5.6 eV, with a variance of approximately 0.23 eV. Further work by Le et al.[19] demonstrated that for a range of metal/water interfaces, the majority of the work function change is induced by Pauli repulsion charge pushback (-1.3 eV for Pt), while the net orientation of water provides only a small contribution across a 10 ps simulation (~0.0-0.2 eV).

Although AIMD studies are able to reproduce the experimental electrochemical properties of the metallic interface, they are computationally costly. This is especially limiting when considering techniques such as microkinetic modelling, where many (tens to hundreds) elementary steps are used to calculate the global kinetics of a complex reaction mechanism.[20] Additional concerns surround the ability of particular GGA functionals (eg. PBE, or other GGA methods) to model the structure of water and solvent metal bond lengths.[21]

In principle, continuum approaches can emulate equilibrium properties of solvent/metal interfaces without extensive configurational sampling. Early work[22] showed that the Poisson-Boltzmann

continuum model was able to capture the qualitative decrease in the work function.[22] However, the original parametrization of the density dependent self-consistent continuum solvation model underestimates the PZC as well as the differential capacitance (DC) for metallic interfaces.[22-23] Hörmann et al. [24] provided an alternative parametrization of the continuum solvent cavity, where the cavity size was reduced to obtain the PZC of the Pt(111)/H_2O interface obtained with AIMD simulation. However, the computational PZC values from the explicit solvent simulation include the orientational contribution of the work function changes, which cannot be represented in the continuum model owing to the absence of atomistic water. Consequently, the dielectric continuum can only induce work function changes through the polarization contributions (ie. electron density changes), which can be over/underestimated depending on the dipole moment of the water layer and the structure of the surface under study. Several publications have suggested including a mono/multilayer of explicit water combined with the dielectric continuum (hybrid implicit/explicit methods) in order to better represent the solvent/metal interface.[25-26] Improvements are apparent for metal oxides, where strong interactions between bonding centers and the atomistic aqueous phase constrain the rotational dynamics of water, which creates a significant dipole moment, thereby introducing a potential offset of up to 1 V to the work function.[26] However, the hybrid method reintroduces the effect of solvent rotational dynamics at the surface, which significantly increases the configurational space which must be sampled to obtain adsorption enthalpies of adsorbates under aqueous conditions.[27] In contrast to metal oxides, water at noble metal surfaces maintains orientational freedom at room temperature, meaning the potential offset due to the overall dipole contribution is far smaller (between -0.1 to 0.2 V).[19, 28] However, as will be later discussed, this value can be overestimated by up to 0.2 V, depending on the method used to measure the computational PZC due to the overestimation of the surface potential of water. We

will show that PZC values for the Pt/continuum interface can be brought closer in line with experiment by parametrizing against the polarization contribution to the atomistic work function change. This is demonstrated by performing an AIMD simulation of the water/Pt(111) interface and extracting work function changes due to changes of the electric dipole moment at the surface. This result is then used to reparametrize the dielectric cavity of the implicit solvent model, representing the work function changes in the absence of orientation effects. We also highlight the quantitative improvements provided by nonlocal van der Waals' (vdW) functionals such as VV10[29] for the PZC. Furthermore, we compare the electronic structure changes of implicit and explicit interfaces through electronic projected d-band density of states (PDOS) for the atoms of the metallic surface.

A further point we wish to address is the use of isodensity cavitation models, which define the dielectric cavity along a specified isocontour of electronic charge. Although these models require the optimization of relatively few parameters, we will demonstrate that no single-value of the isodensity can simultaneously give accurate solvation energies for small molecules and metallic work function changes. This is a consequence of homogeneously applying the isodensity parameter across the whole system, combined with the large deviations from the default cavity parameters necessary to obtain accurate values of the PZC.[24] Such changes in the cavity shape compromise the accuracy of the solvation free energy ΔG_{solv} for species containing light elements, as the default isodensity values are selected to minimize the error of solvation energy changes for common organic molecules. However, cavitation schemes such as the soft sphere radii of Fisicaro et al.[30] allow one to define separate cavity radii for surface metal species and first row elements. Using the capability, we demonstrate for the first time the ability of the soft sphere model to capture

simultaneously the aqueous enthalpy of adsorption of phenol on Pt(111), as well as the solvent work function of the metallic surface.

2 Methods

2.1 ONETEP Calculations

Calculations were performed with ONETEP,[31] a linear-scaling DFT code. ONETEP is based on a linear-scaling reformulation of DFT in terms of the one-particle density matrix which is expressed via atom-centered non-orthogonal generalized Wannier functions (NGWFs). The NGWFs are expanded in term of a basis set of periodic sinc (psinc) functions which are related to plane waves via a unitary transformation. By truncating the NGWFs and the density matrix beyond certain radii, we can perform DFT calculations with computational effort which is reduced (or linear for large enough systems) as a function of the number of atoms, taking practical advantage of the principle of near-sightedness of electronic matter of Walter Kohn.[32] Thus ONETEP allows calculations of much larger scale than conventional DFT approaches, as such approaches are limited to smaller scales because the computational effort increases with the third power in the number of atoms. In ONETEP simulations of metallic systems were carried out with the finite temperature Kohn-Sham DFT approach of Mermin[33] which is implemented as a variant of the Ensemble DFT method of Marzari[34], which has been reformulated for the localized NGWF framework of ONETEP.[35]

The PBE[36] GGA exchange-correlation functional and the nonlocal vdW correction including functional rVV10[29] were used throughout this work. The core states were represented by Projected Augmented Waves (PAW),[37] obtained from the GBRV pseudopotential library.[38] The valence states of the Pt atoms were represented using 12 NGWFs in spherical regions of radii 9.0 a_0, with

an electronic configuration of $5p^6 6s^1 5d^9 6p^0$, following the work of Verga et al.[39]. The psinc kinetic energy cut-off was set to 850 eV for total energy calculations. Geometry relaxations[40] were conducted with the BFGS algorithm,[41] using a convergence threshold of 5×10^{-3} E_h/a_0 for the maximum force. A Fermi-Dirac smearing width of 0.09 eV is used throughout for the electronic occupancies. For systems including explicit water, the slab type Coulomb cut-off approach was used[42-44] to eliminate electrostatic interactions perpendicular to the slabs. The cut-off is applied to both the electronic density and the longrange tail of the local pseudopotentials, while the ion-ion Coulomb energy is calculated through a quasi-2D Ewald summation.[45]

Comparisons to previous benchmark properties for both the Pt fcc bulk and Pt(111) surface in vacuum are provided in the Supporting Information (SI) S2-S4.

2.2 CP2K Calculations and ab initio molecular dynamics

CP2K[46] electronic structure calculations were conducted using the PBE GGA exchange-correlation functional[40] corrected with D3-type van der Waals potentials[47] for dispersion interactions. We employed the GPW hybrid basis set scheme[48] in which the Gaussian basis sets of DVZP (for the Pt bulk and Pt surface without water) and TZVP (for a water film on Pt(111)) quality were used to expand the Kohn-Sham states and a plane wave energy cut-off of 450 Ry was used for electrostatics calculations.

An AIMD simulation was conducted within the NVT ensemble, with the temperature enforced with a velocity-rescaling thermostat.[49] We used modified masses (5 au for H, and 10 au for O) and a time step of 1 fs to integrate the equations of motion. We used a frame of a system containing 64 Pt atoms and 52 water molecules, published in a previous work[12]. The system was initially mixed with a 2 ps run at T=1000 K, and subsequently cooled down to 330 K. This was followed with a

production run of 24 ps, at T = 330K. The temperature of 330 K ensures overstructuring of the water layer is avoided, which is otherwise known to arise in simulations of liquid water using the PBE functional.[50] We should note that, due to the use of modified masses, which enables better sampling on a shorter trajectory, the dynamics quantities considered in sections S6 and S7 do not correspond to the actual correlation time of water at the Pt(111) surface. Rather they serve as a measure of the convergence of the calculations with respect to the characteristic time constant of the system. Our use of CP2K was motivated by a desire to maintain consistency with our previous simulations of metal/water interfaces.[12] The resulting structures were eventually used as explicit solvent systems to study the electronic structure and calculate the work function. These calculations were performed in ONETEP, allowing for consistent comparison between the explicit and implicit solvent models.

2.3 Continuum Solvent Model

The continuum solvent model used in this work utilizes the Poisson-Boltzmann method formulated by Fattebert, Gygi and Scherlis (FGS).[51-53] This was implemented with additional dispersion and repulsion terms into ONETEP by Dziedzic et al.[43], providing quantitative improvement for the solvation free energy for neutrals, anions and cations. Solutions to the Poisson-Boltzmann problem are obtained with the parallel multigrid DL_MG library.[54]

The key feature of the FGS formulation is the definition of the dielectric cavity, which is constructed as a function of the electron density,

$$\varepsilon\big(\rho(\boldsymbol{r})\big) = 1 + \frac{\varepsilon_\infty - 1}{2}\left[1 + \frac{1 - (\rho(r)/\rho_0)^{2\beta}}{1 + (\rho(r)/\rho_0)^{2\beta}}\right], (1)$$

where the dielectric permittivity smoothly transitions from 1 to ε_∞, which can be adjusted to the bulk value of the solvent (1 to 78.56 in the case of water). The cavity boundary is specified by the parameters: ρ_0, which defines the midpoint of the cavity function (ie. the isocontour of charge density where $\varepsilon\big(\rho(\boldsymbol{r})\big) = \frac{\varepsilon_\infty}{2}$); and β, which modulates the steepness of the transition from vacuum

to bulk dielectric permittivity. The default parameters are taken as $\rho_0 = 0.00035$ eV Å^{-3} and $\beta = 1.3$, which were obtained by minimizing the error of the free energy of solvation for a set of neutral, cationic and anionic species.[55]

We will compare the FGS dielectric model with the soft sphere cavitation model of Fisicaro *et al.*[30] This model defines the dielectric cavity through interlocking spheres defined by a set of distance-dependent functions:

$$\varepsilon(\boldsymbol{r}_i, \{\boldsymbol{R}_i\}) = (\varepsilon_\infty - 1)\{\prod_i h(\{\xi\};\ \|\boldsymbol{r} - \boldsymbol{R}_i\|)\} + 1, \quad (2)$$

where $\|\boldsymbol{r} - \boldsymbol{R}_i\|$ defines the distance to a point at position $\boldsymbol{r}$ from atomic center $\boldsymbol{R}_i$, ε_∞ the dielectric permittivity of the bulk solvent, and $\{\xi\}$ the parameters for a specific atomic center. The *h* functions define a set of atom centered error functions, *erf*, smoothly varying from 0 to 1:

$$h(\boldsymbol{r_i}, \boldsymbol{\Delta}, \|\boldsymbol{r} - \boldsymbol{R}_i\|) = \frac{1}{2}\left[1 + erf\left(\frac{\|\boldsymbol{r} - \boldsymbol{R_i}\| - \boldsymbol{r_i}}{\Delta}\right)\right], \quad (3)$$

where $\boldsymbol{\Delta}$ defines how quickly the dielectric function varies from the bulk to vacuum permittivity values and $\boldsymbol{r_i}$ the distance defines the midpoint of the dielectric function for atomic center *i*.

The parameters $\boldsymbol{r_i}$ and Δ are determined using a similar error minimization procedure as outlined in the original soft-sphere scheme.[45] We use the vdW radii of Alvarez,[56] $\mathbf{r_{vdW}}$, and multiply this set of radii by a scaling factor, *f*, in order to uniformly increase/decrease the soft sphere radii ($\boldsymbol{r_i} = f\boldsymbol{r_{vdW}}$). The scaling value was varied from *f* = 1.0 to 1.4 to attain a minimum mean absolute error (MAE) for the free solvation, ΔG_{solv}. This was performed over a set of 20 neutral molecules containing a range of common functional groups, and results were compared to experimental data obtained from the Minnesota Solvation Database.[57] The lowest MAE (1.09 kcal mol^{-1}) was attained for $\Delta = 0.5$ with a scaling factor of *f* = 1.33.

To demonstrate the sensitivity of the work function of a Pt(111) surface to variations in cavity size, the values of ρ_0 and $\boldsymbol{r_i}$ (for Pt) were varied between 0.0035-0.04 e/Å^3 and 3.90-5.20 a_0 for

each respective cavitation model. To ensure that solvent dielectric was excluded from the inside of the Pt slab, we manually set $\varepsilon(\boldsymbol{r})$ to 1.0 from the bottom to the top layer of the metallic slab.

2.4 Work Function Changes in Solvent

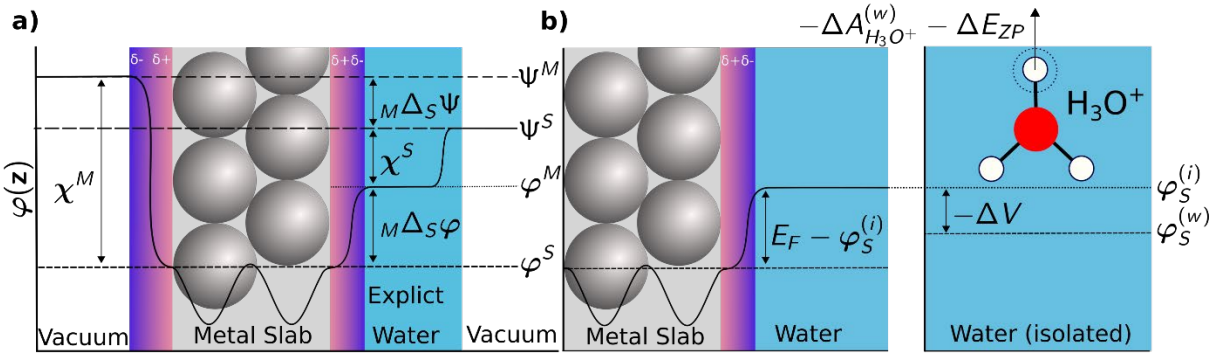

Figure 1: The variation of the electrostatic potential averaged in the xy-plane ($\varphi(\mathbf{z})$) for a metallic slab interfaced with solvent and vacuum. φ and shows the inner potential, Two methods of calculating the PZC are: a) The work function method, where the difference between the outer (Volta) potentials of the solvent (ψ^S) and metallic surface (ψ^M) represents the work function change. χ is the surface potential of the indicated phase. b) The Computational Standard Hydrogen Electrode method, where the Fermi level (E_F) is referenced to the inner potential of water $\varphi_S^{(i)}$. The electrode is converted to the SHE scale by coupling $E_F-\varphi_S^{(i)}$ to the free energy of deprotation for the hydronium cation calculated in a pure water box, taking into account the zero-point energy of the H-OH_2^+ bond ($\Delta_{DP}A^{(w)}_{H_3O^+}-\Delta E_{ZP}$). Defects of the PBC between the two cells are eliminated by subtracting the difference between the bulk electrostatic potentials of water (ΔV).

The work function of the bare and solvated metallic slabs can be expressed in terms of absolute potentials (Figure 1)[25, 58]:

$$\phi^M \equiv U_M = -\frac{\mu^M}{e} + \chi^M, (4)$$

$$\phi^{M|S} \equiv U_{M|S} = {}_S\Delta_M\varphi - \frac{\mu^M}{e} + \chi^S, (5)$$

Where ${}_S\Delta_M\varphi$ is the Galvanic potential difference between the solvent and the metal, $\frac{\mu^M}{e_0}$ is the standard potential of the electron in the metallic species, e is the elementary charge of an electron and χ^S is the surface potential at the solvent/vacuum interface.

The inner (Galvanic) potential of solvent and the metallic bulk (φ^S and φ^M) are taken as the average of the single particle electrostatic potential through the xy-plane for a selected section of the phase, while the outer (Volta) potential ($-e_0\psi$) represents the single particle electrostatic potential averaged across a plane vacuum outside of the phase indicated by the superscript. The surface potential for either phase (shown as α), χ^α therefore represents the work required to move a particle with elementary charge through the interface between the measured phase and vacuum:

$$\chi^\alpha = \psi^\alpha - \varphi^\alpha, (6)$$

From this, the total change in the work function ($\Delta\phi_{tot} = \phi^{M|S} - \phi^M$) can be expressed as the change in the outer potential in the vacuum region of both phases:

$$\Delta\phi_{tot} \equiv {}_S\Delta_M\varphi + \chi^M - \chi^S = \psi^M - \psi^S \equiv {}_S\Delta_M\psi, (7)$$

In addition to the surface potential of the solvent/vacuum interface χ^S, the solvent layer introduces an additional potential step between the metal and the bulk of water (${}_S\Delta_M\varphi$). This represents the contribution to $\Delta\phi_{tot}$ from: a) electron density changes produced by charge transfer or Pauli repulsion mechanisms at the surface; or b) The intrinsic dipole of the solvent at the surface.[16] According to the theory of Trasatti,[59] these two contributions give the total work function change,

$$\Delta\phi_{tot} = \phi^{Pt|S} - \phi^{Pt} = \Delta\phi_{pol} + \Delta\phi_{orient}, (8)$$

where $\Delta\phi_{\mathrm{orient}}$ arises from the net dipole moment of the solvent at the metallic surface, and $\Delta\phi_{\mathrm{pol}}$ arises from changes of the electronic structure of the metallic surface. $\Delta\phi_{\mathrm{pol}}$ was obtained by subtracting $\Delta\phi_{\mathrm{orient}}$ from the total work function change. For individual configurations of the AIMD simulation, $\Delta\phi_{\mathrm{orient}}$ is calculated by performing a separate single point calculation of the frozen water configuration isolated from the metallic slab and taking the Volta potential difference between the vacuum regions either side of the bulk water.

2.5 Calculating the Potential of Zero Charge

The potential of zero charge of a surface vs. the standard hydrogen electrode, $U_{PZC}(SHE)$ is calculated by coupling the electrode under study,

$M{\cdot}(aq) + e^{-}(vac) \rightarrow M^{-}(aq)$, (9)

to the redox half reaction of the proton,

$H^{+}(aq) + e^{-}(vac) \rightarrow \frac{1}{2}H_2(g)$, (10)

To give the overall electrode reaction,

$M^{-}(aq) + H^{+}(aq) \rightarrow \frac{1}{2}H_2(g) + M{\cdot}(aq)$. (11)

In *ab initio* calculations, the overall potential of this equation can be calculated through either a) The work function method or b) The Computational Standard Hydrogen Electrode (CSHE).

In the work function method, $U_{PZC}(SHE)$ is calculated as the difference between the absolute potentials of the two half equations (eq. 9 and 10) referenced against vacuum,[58]

$U_{PZC}(SHE) = U_{M|S}(abs) - U^{o}_{H^{+}/H_2}(abs)$, (12)

where,

$U_{M|S}(abs) = {}_{S}\Delta_{M}\varphi - \frac{\mu^{M}}{e} + \chi^{S}_{calc}$, (13)

and,

$$U^{o}_{H^+/H_2}(abs) = \frac{\mu^{o}_{H^+} - \frac{1}{2}\mu^{o}_{H_2}}{e} + \chi^{S}_{exp}, \text{(14)}$$

where $U^{o}_{H^+/H_2}(abs)$ is taken as the experimentally determined value of Trasatti,[15] 4.44 V, $U_{M|S}(abs)$ is taken as the work function of the metallic/water interface, and χ^{S}_{calc} and χ^{S}_{exp} are the *ab initio* and experimentally determined surface potentials of water.

In contrast, the CSHE approach[19, 58, 60] calculates $U_{PZC}(SHE)$ by directly computing the free energy difference between the redox equations (eq. 9 and 10), where eq. 9 is expressed as two steps,

$$H^+(aq) \rightarrow H^+(g), \text{(15)}$$

$$H^+(g) + e^-(vac) \rightarrow \frac{1}{2}H_2(g). \text{(16)}$$

The electrode potential vs. the SHE is then calculated as,

$$eU^{o}_{PZC} = -E_F - e(\varphi^{(w)}_{wat} - \varphi^{(i)}_{wat}) + \Delta_{DP}A^{(w)}_{H_3O^+} - \mu^{g,o}_{H^+} - \Delta E_{ZP}\ , \text{(17)}$$

where E_F is the Fermi Level of the metallic slab and φ_{wat} is the average electrostatic potential of bulk water, with $\varphi^{(i)}_{wat}$ and $\varphi^{(w)}_{wat}$ measured for a water box in the presence of the metallic slab a pure water box respectively ($\varphi^{(w)}_{wat} = 0$). $\Delta_{DP}A^{(w)}_{H_3O^+}$ (15.35 eV)[60-61] is the free energy of deprotonation of the hydronium cation calculated *via* Free Energy Perturbation for the insertion of a proton into bulk water, $\mu^{g,o}_{H^+}$ (15.81 eV)[62] is the standard chemical potential of the H^+ ion, and ΔE_{ZP} (0.35 eV)[63] is the zero point energy of the H-OH_2^+ bond. $e(\varphi^{(w)}_{wat} - \varphi^{(i)}_{wat})$ is required to correct the uncertainty in the potential reference (Hartree Potential Shift) of $\Delta_{DP}A^{(i)}_{H_3O^+}$ in the metallic/water system relative to the measured value of $\Delta_{DP}A^{(w)}_{H_3O^+}$, where,

$$\Delta_{DP}A^{(i)}_{H_3O^+} = \Delta_{DP}A^{(w)}_{H_3O^+} + e(\varphi^{(w)}_{wat} - \varphi^{(i)}_{wat})\ , \text{(18)}$$

In terms of the redox equations, $\Delta_{DP}A^{(w)}_{H_3O^+} - \mu^{g,o}_{H^+} - \Delta E_{ZP}$ now correspond to the free energy change of eq. 15 and 16, and $-E_F - e(\varphi^{(w)}_{wat} - \varphi^{(i)}_{wat})$ corresponds to vertical ionization energy of the metallic surface corrected for the Hartree Potential Shift.

To allow comparison of $\Delta\phi_{\mathrm{tot}}$ and $\Delta\phi_{\mathrm{orient}}$ between the work function and CSHE methods, we can recover $\phi^{\mathrm{Pt|S}}$ with the following expression:

$$\phi^{\mathrm{Pt|S}} = (eU^{o}_{PZC} + U^{o}_{H^+/\,H_2}(abs)), \quad (19)$$

which converts the potential vs. the SHE to the absolute potential scale. Furthermore, we obtain $\Delta\phi_{\mathrm{orient}}$ by assuming that $\Delta\phi_{\mathrm{pol}}$ is equal between the two methods and re-adding its contribution to $\Delta\phi_{\mathrm{tot}}$.

3 Results and Discussion

3.1 Explicit Solvent Work Function Changes

In order to correctly parameterize the work function changes of Pt(111) with the implicit solvent model, we first obtained the value of $\Delta\phi_{\mathrm{tot}}$ in explicit solvent. This was achieved by averaging 90 evenly spaced snapshots (sampled every 0.25 ps) from an equilibrated 24 ps AIMD run performed at T = 330 K (Table 1). We analyzed the molecular density and orientation dynamics water molecules within the double layers to validate the convergence of our simulations (details provided in S5).

Table 1: Interface work function values, $\phi^{\mathrm{Pt|S}}$, where the values in this work are obtained from an average of 90 snapshots from a 24 ps AIMD calculation. $\Delta\phi_{\mathrm{tot}}$ is calculated relative to the work function of the system in vacuum found in each respective work. The work function due to charge

rearrangement, $\Delta\phi_{pol}$ is measured as the change in dipole due to the change in electron density between the vacuum and solvent system. U_{pzc} is calculated relative to the absolute SHE of *Trasatti*,[15] $U^{o}_{H^+/H_2}(abs) = 4.44\ V$. Errors are calculated as 95% confidence intervals.

	ϕ^{Pt} / eV	$\phi^{Pt|S}$ / eV	$\Delta\phi_{tot}$ / eV	$\Delta\phi_{orient}$/ eV	$\Delta\phi_{pol}$ / eV	U_{PZC} / V
WF Method (PBE)	5.61	4.83 ± 0.13	-0.73 ± 0.13	$+0.50 \pm 0.13$	-1.23 ± 0.03	0.43 ± 0.13
CSHE (PBE)	5.83	4.65 ± 0.08	-0.95 ± 0.08	$+0.28 \pm 0.08$	-1.23 ± 0.03	0.21 ± 0.08
WF Method (rVV10)	5.83	5.00 ± 0.13	-0.83 ± 0.13	$+0.49 \pm 0.03$	-1.32 ± 0.03	0.56 ± 0.13
CSHE (rVV10)	5.83	4.80 ± 0.08	-1.03 ± 0.08	$+0.29 \pm 0.08$	-1.32 ± 0.03	0.36 ± 0.08
WF Method[a]	5.51	4.96 ± 0.01	-0.55	$+0.7$	-1.25	0.52 ± 0.01
CSHE[b]	5.8	4.7[f]	-1.1	$+0.2$	-1.3	0.2
Experiment	5.9	–	–	–	-	0.3[c] / 0.33[d]

[a] Sakong et al. [17] ($Pt(6x6)/(H_2O)_{144}$), 298 K, RPBE+D3. [b] Le et al.[19] (calculated using the Computational SHE method), 330 K, PBE+D3. [c] ref.[11], CO-adsorption technique. [d] ref.[64], CO-adsorption technique [e] Value obtaining by adding $U^{o}_{H^+/H_2}(abs)$ to calculated U_{PZC}(SHE).

The value of U^{o}_{PZC} calculated with the work function method coincides within 0.1 V of previous studies using the same approach but is systematically larger than the computational SHE value by up to 0.2 V for both PBE and rVV10. As each study is well statistically sampled, this suggests a fundamental discrepancy between the methods used to calculate U^{o}_{PZC}.

The key difference between the work function and computational SHE methods is the treatment of the surface potential, χ^S. It is assumed the two values of χ^S exactly cancel (ie. $\chi^S_{calc} - \chi^S_{exp} = 0$) in the case in both experiment and the CSHE method. However, in the work function method

(eq. 12-14), the value of χ^S calculated implicitly in $U_{PZC}(\text{abs})$ (χ^S_{calc}) and measured experimentally in $U^o_{H^+/H_2}(\text{abs})$ (χ^S_{exp}) no longer exactly match, as χ^S_{calc} is determined by the dipole moment of the water/vacuum interface in the AIMD simulation. χ^S_{calc} varies between 0.15-0.33 V in the literature,[26, 65] whereas χ^S_{exp} is measured between 0.13-0.14 V.[15, 66] Therefore in the work function method, the contribution from $\Delta\phi_{orient}$ to $\Delta\phi_{tot}$ can be overestimated by up to 0.3 V, which arises through the additional contribution to $\Delta\phi_{orient}$ from $\chi^S_{calc} - \chi^S_{exp}$. In contrast, the CSHE method removes the influence of χ^S by referencing the Fermi Level to the bulk electrostatic potential of water as opposed to the vacuum potential. This results in a lower value of U_{PZC}(SHE) for the CSHE method compared to the work function method (0.21 V vs. 0.43 V for PBE), where $\Delta\phi_{orient}$ was +0.5 eV and +0.3 for the work function and CSHE methods respectively. We therefore draw a similar conclusion to Le et al., where the contribution of $\Delta\phi_{orient}$ to U_{PZC} is relatively small compared to $\Delta\phi_{pol}$.

In contrast, $\Delta\phi_{pol}$, is independent of the reference used for the electronic energies, as evidenced by the small quantitative differences between the two methods calculating U_{PZC}(SHE). Furthermore, $\Delta\phi_{pol}$ exhibits a small variance (σ = 0.01 eV) compared to $\Delta\phi_{tot}$ (σ = 0.43 eV). This is a consequence of the rotational freedom of the water molecules across the simulation, which drives the variation of $\Delta\phi_{orient}$, whereas $\Delta\phi_{pol}$ largely varies as a result of distance of the Pt-H_2O bonds as argued by Tripkovic.[14]

The exchange rate of water molecules between the interfacial layer and the rest of the liquid occurs approximately one every 0.25 ps (see S7), indicating these events are accessible on the 24 ps time scale of the current simulation. On the other hand, water dipole orientation relaxation occurs on the ~10.7 ps time scale (see S6) such that we are able to observe more than 2 relaxation

events per molecule during our simulation. This indicates that our current simulation accounts for the critical time scale at which the metal/water interface structure changes and impacts upon $\Delta\phi$.

The dynamics in CP2K were performed with the PBE functional with the Grimme D3 dispersion correction, while the snapshots were assessed with nonlocal and empirical vdW correction schemes (ie. The rVV10 functional). The empirical approach provides no correction for the nonlocal density changes due to dispersion, meaning density dependent properties (ie. The work function) assessed with pure PBE and PBE+D3 would be identical to one another for the same structure. However, including the rVV10 functional demonstrates that the nonlocal vdW correction systematically increases the work function and U_{PZC}(SHE) for the Pt(111) surface. We should however note that the description of the structure and dynamics of water varies slightly between these two vdW corrections, particularly at the vacuum air interface.[67] The use of rVV10 as opposed to PBE+D3 for the dynamics may therefore have some impact on the value of $\Delta\phi_{\mathrm{orient}}$ calculated with rVV10 unaccounted for in this work.

3.2 Implicit Solvent Work Function Changes

Previous studies show that water at the Pt surface forms a 5 Å bi-layer with a small orientational dipole.[19, 28] Therefore, provided the contribution from $\Delta\phi_{\mathrm{orient}}$ remains small, the continuum solvent approach can represent the overall work function change in solvent with reasonable accuracy, with an error similar in scale to AIMD studies. This section will outline the parameters required to reproduce the work function changes of molecular water with the continuum model. This will be achieved using two cavitation models outlined in the Methods section.

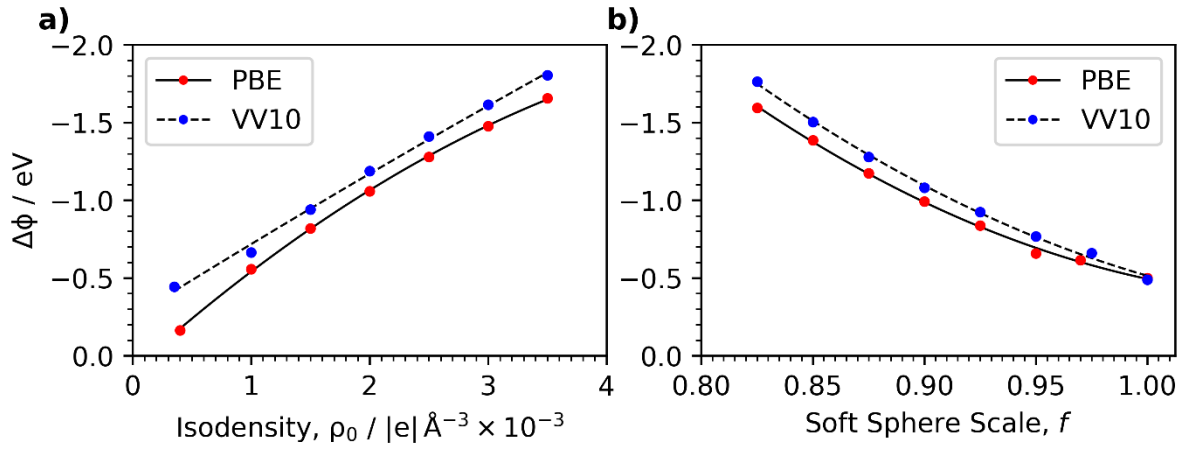

Figure 2: Variation of Δϕ with differing cavity parameters for a Pt(7×6×4) slab: a) Isodensity of the FGS model and b) Scaling factor of the soft sphere model with respect to the default Pt radius of 2.29 Å. Line fitting is performed with a second degree polynomial.

The default parametrization of the isodensity model reproduces the qualitative decrease in the work function (-0.16 eV). This is significantly smaller than the 1.23 eV decrease calculated from the explicit solvent systems using PBE. However, by defining the isodensity, ρ_0 or the soft sphere radii such that the bulk dielectric is drawn closer to the atomic centers, the work function decrease can be brought into closer agreement with the explicit approach. This occurs through increased charge re-arrangement towards the surface, which decreases the dipole moment of the metallic centers and the diffuse electron region, resulting in greater reductions of the work function. Careful tuning of the cavity parameters and polynomial fitting then obtain quantitative agreement with the average work function of the explicit solvent systems (Figure 2 and Table 2). We show that this is achieved with ρ_0 = 0.0024 for the isodensity approach and a scaling factor of 0.87 for the soft sphere of Pt (corresponding to $\mathbf{r_{vdW}}$ = 1.99 Å) for PBE.[26, 58]

Table 2: Default parameters of the isodensity and the soft sphere model cavity model, and the values from a second-order polynomial fitting of the cavity parameters for a Pt(7×6×4) slab (Figure 2) corresponding to the average electronic change in the work function ($\Delta\phi_{pol}$ = -1.23 eV (PBE) / -1.32 eV (rVV10)) of the AIMD snapshots, for an initial work function of 5.71 eV (PBE) and 5.91 eV (rVV10). The corresponding values of the PZC are also presented against the absolute SHE scale.

Cavity Model	Soft Sphere Scale (f)	FGS (ρ_0)	U_{PZC}(SHE) / V
Default	1.33	0.00035	-
Re-fitted (PBE)	0.867	0.00237	0.04
Re-fitted (rVV10)	0.872	0.00213	0.15
Ref[24]	-	-	0.52
Experiment[11]	-	-	0.29

Previous studies parametrized the cavity sizes against the PZC of AIMD simulations using the work function method, yielding a PZC of 0.5 V vs. SHE for Pt(111).[17-18] Excluding the overestimated orientation effects decreases the calculated PZC, where results obtained with rVV10 result in greater quantitative agreement with experiment (Table 2). Furthermore, the use of a larger slab to parametrize these results leads to an upward shift of 0.1 eV relative to the explicit solvent results.

We note that by using this parametrization scheme, the value of U_{PZC}(SHE) for the dielectric interface should be offset by approximately -0.2-0.3 V from experiment/CSHE and up to -0.5 V with respect to the work function method, depending on the calculated value of $\Delta\phi_{orient}$.[26] Although one can represent the orientation contribution by including an explicit layer at the

metallic surface, one would require dynamic sampling to obtain an accurate value of χ^S_{calc} which would correctly cancel χ^S_{exp}.

3.3 Dispersion Including Functionals and the Work Function

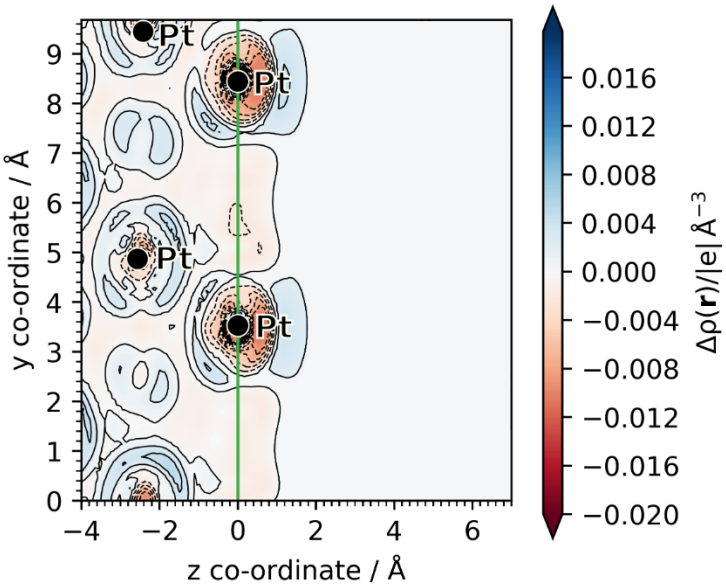

Figure 3: Electron density difference profile between the rVV10 and PBE functionals for the Pt(111) surface (taken from a single snapshot from the 24 ps AIMD simulation). Blue regions represent electronic charge accumulation and red charge depletion. First layer of the Pt atoms is taken as z = 0. The green line represents the [111] plane at the vacuum interface.

The PBE GGA functional systematically underestimates the vacuum work function compared to the experimental measurements (5.7 vs. 6.0 eV for Pt(111)). However, the dispersion including functional rVV10 systematically increases the work function of the Pt(111) slab in vacuum, bringing the value more in line with experimental LEED studies. By analyzing the change in electron density $\Delta\rho(\mathbf{r})$ for a simple Pt surface, as shown in Figure 3, we observe that the rVV10 functional redistributes charge towards the vacuum. This increases the surface dipole, which in

turn increases the work function. In vacuum, the work function of the Pt(7×6×4) surface increases from 5.7 eV to 5.9 eV, similar to observations made by Patra et al.[68].

Values of $U_{PZC}(\mathrm{SHE})$ obtained with the PBE functional for the implicit solvent interface are significantly underestimated with respect to experiment (0.0 vs. 0.3 V). However, Figure 2 shows that the work function changes induced by the implicit solvent for PBE and rVV10 closely align. As a result, the inclusion of van der Waals interactions functional increases the calculated values of $\mathrm{U_{PZC}(SHE)}$ by approximately 0.2 V, thereby improving agreement with experiment. Furthermore, meta-GGAs in conjunction with the rVV10 correction lead to greater quantitative increases in the work function,[68] therefore we anticipate that functionals such as SCAN+rVV10 would further improve the description of the diffuse electron region.

3.4 Energetics of Adsorption for Phenol on Pt(111)

The key advantage of the soft sphere model over the isodensity model is ability to define the cavity size for individual atoms. The importance of this is highlighted when considering the free energies of solvation of simple molecules on the metallic surface.

As shown in Table 3, increasing ρ_0 values lead to worsening errors for the solvation enthalpy ΔH_{solv} of phenol. (We note that ΔH_{solv} is calculated as ΔG_{solv} in ONETEP, which includes both cavitation and dispersion repulsion contributions.[43] These terms contain a significant portion of the solvation enthalpy which cannot be trivially separated from the relatively small entropy contribution. Therefore, these terms are included and calculated values are quoted as ΔH_{solv} for ease of comparison with experimental enthalpy values). Considering that the isodensity values are parametrized to minimize the solvation free energy error for neutral, cationic and anionic species, it is unsurprising that deviations from the default ρ_0 value leads to worsening errors. As a consequence, accurate values of both solvation free energies and the metallic work function cannot

be computed with the isodensity model. In contrast, the soft sphere model radii can be separately defined for metallic and organic species cavity functions, meaning these quantities can be calculated simultaneously.

Table 3: Solvation enthalpy ΔH_{solv} for phenol and Pt(111) with the isodensity and soft sphere models, with the refitted cavity parameters obtained in Section 3.4. All values in kJ mol^{-1} and obtained with the rVV10 functional.

Cavity Model	Phenol	Pt(111) (per atom)
Isodensity (Default)	-31.7	-0.24
Isodensity (Refitted)	-206.6	-27.66
Soft Sphere (Default)	-22.3	0.61
Soft Sphere (Refitted)	-22.3	-16.90
Expt.[a]	-28.9	-9.61[b]

[a] Minnesota Solvation Database.[57] [b] Calculated using the energy of adhesion of solid water to the Pt surface and the surface energy of water (See SI S8).

The lack of solvation free energy data for transition metal surfaces limits the comparisons that can be made with experiment. However, using a simple modification of the bond additivity model,[69] one can obtain an approximation of ΔH_{solv} for a single Pt atom of Pt(111) (See SI S8 and ref[69]). This allows for qualitative assessment of the refitted cavity parameters (Table 3). The default cavity parameters significantly underestimate the effect of solvation, to the point where energetically unfavorable cavitation/dispersion-repulsion effects dominate over polarization in the case of the soft sphere model. By drawing the cavity closer to the metallic atoms, the effect of the

dielectric continuum is significantly increased. However, both cavitation methods oversolvate the surface Pt atoms, where the refitted soft sphere parameter facilitates agreement to within 7 kJmol^{-1}. The refitted isodensity parameter significantly overestimates the solvation enthalpy by 18 kJ mol^{-1}, despite yielding the same value of the work function as the isodensity model. This suggests that the topology of the cavity has significant effect on the solvation energy changes. We note however in the case of the soft sphere model, a compromise cavity radius may be found to give adequate agreement with both solvation and work function changes.

To demonstrate the flexibility of the soft sphere approach, we performed a series of calculations to obtain the enthalpic changes for the adsorption of phenol on the Pt(111) surface under aqueous and vacuum conditions (Scheme 1). Enthalpy changes are compared to the bond-additivity analysis conducted by Singh and Campbell.[69] (Table 4).

Scheme 1: Thermodynamic cycle for the adsorption of phenol on a Pt(6x6x4) facet under implicit aqueous conditions and in vacuum. ΔH_{solv}^{int} and $\Delta H_{solv}^{non-int}$ describes the enthalpy of solvation for the interacting and non-interacting metal/phenol systems. Values found in Table 4 and Table S6.

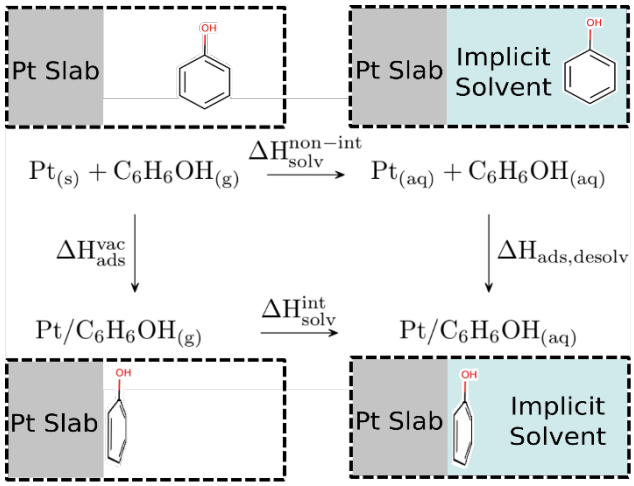

Table 4: Enthalpy changes outlined in Scheme 1 for the adsorption of phenol to the Pt(111) (Pt(6x6x4)) facet under aqueous conditions (All values in SI Table S6). Calculations were performed with the re-fitted cavity parameters obtained in Section 3.4 for both soft sphere and isodensity methods. $\Delta H_{desolv}^{phenol+slab}$ shows the enthalpy change associated with the desolvation of the slab and phenol upon adsorption. ΔH_{ads}^{aq} corresponds to the heat of adsorption under aqueous conditions. All values in kJ mol^{-1}.

Cavitation Model	ΔH_{ads}^{vac}	$\Delta H_{ads,desolv}$	$\Delta H_{desolv}^{phenol+slab}$	ΔH_{ads}^{aq}
PBE (Isodensity)	-122.88	36.88	-317.36	-280.49
PBE (Soft Sphere)		29.09	-134.03	-104.94
rVV10 (Isodensity)	-188.69	-48.50	-269.88	-318.38
rVV10 (Soft Sphere)		-35.51	-141.42	-176.93
Bond-Additivity Model[69]	-200.0[70,b]	-21.0[5,a]	-116.0	-148.4[a]/ -200.0[b]

[a] High-coverage Pt/phenol bond energy value. [b] Approximated low coverage Pt/phenol bond energy.

Enthalpies of adsorption for phenol (ΔH_{ads}^{vac}) were significantly underestimated by the PBE functional (-122.88 kJ mol^{-1} vs. ~-200 kJ mol^{-1}). This leads to qualitatively incorrect outcomes, where the low Pt/phenol bond energy results in an endothermic enthalpy for $\Delta H_{ads,desolv}$. Calculations performed with rVV10 substantially improved agreement with experimental values of ΔH_{ads}^{vac} (-188.69 kJ mol^{-1} vs. ~ -200.0 kJ mol^{-1}), which in turn restores the correct exothermic enthalpy of $\Delta H_{ads,desolv}$.

We aim to compare computed values of ΔH_{ads}^{aq} to values obtained through bond-additivity analysis. To achieve this, $\Delta H_{ads,desolv}$ was decomposed into enthalpy changes from three sources: (1) adsorption of phenol to Pt(111) under aqueous conditions, $-\Delta H_{ads}^{aq}$ (2) desolvation of the occupied Pt atoms, $-\Delta H_{desolv}^{slab}$ and (3) desolvation of one face of phenol, $-\Delta H_{desolv}^{phenol}$,

$$-\Delta H_{ads,desolv} \approx -\Delta H_{ads}^{aq} - \Delta H_{desolv}^{slab} - \Delta H_{desolv}^{phenol}, \quad (20)$$

where $-\Delta H_{desolv}^{slab} - \Delta H_{desolv}^{phenol} = -\Delta H_{desolv}^{phenol+slab}$ (Table 4). Values of $-\Delta H_{desolv}^{phenol+slab}$ were obtained through two approximations. Similar to the explicit system, adsorbed phenol and its dielectric cavity 'displaces' the implicit solvent from the metallic surface. As phenol adsorbs planar to the Pt surface, the solvation energy lost for the metallic slab can be approximated as a proportion of the metallic slab the dielectric cavity of phenol occupies in the xy-plane multiplied by the total solvation of the metallic slab,

$$-\Delta H_{desolv}^{slab} \approx \frac{\text{area of phenol cavity}}{\text{area of Pt surface}} \times \Delta H_{solv}^{slab}, \quad (20)$$

where the proportions are listed in SI S9. A further approximation can be made for $\Delta H_{desolv}^{phenol}$ by considering the flat lying adsorption geometry of the molecule with only one side facing the implicit solvent, therefore desolvation can be simplified as $-\Delta H_{desolv}^{phenol} \approx \frac{1}{2} \times \Delta H_{solv}^{phenol}$.

Bond additivity analysis calculated a ~57 kJ mol^{-1} discrepancy between experimental values of ΔH_{ads}^{vac} and derived values of ΔH_{ads}^{solv}. However, it has been suggested phenol adopts high local coverages on Pt(111) under aqueous conditions.[71] In vacuum, higher coverage reduces adsorption strength from ~-200 kJ mol^{-1} to ~-142 kJ mol^{-1},[70] which suggests the difference between ΔH_{ads}^{aq} and ΔH_{ads}^{vac} results from coverage effects rather than an intrinsic weakening of Pt/phenol bonding. As our calculations are performed with low phenol coverage, one should we therefore expect ΔH_{ads}^{aq} to be approximately equal to ΔH_{ads}^{vac}. Calculations using the soft sphere

model support these findings, where the difference between ΔH_{ads}^{aq} and ΔH_{ads}^{vac} is correspondingly small (+17.95 kJ mol^{-1} and +11.76 kJ mol^{-1} for PBE and rVV10 respectively). In contrast, the same difference obtained with isodensity cavitation is substantially larger (-157.60 kJ mol^{-1} (PBE) and -129.70 kJmol^{-1} (rVV10)), largely as a result of the overestimated value of $\Delta H_{desolv}^{phenol}$. This is a consequence of readjusting the ρ_0 cavity parameter, which places the dielectric too closely to the phenol molecule. The soft sphere model circumvents this by maintaining the default cavity size of phenol, while using the newly parametrized cavity radii for Pt from Section 3.4.

It should be noted that the soft sphere model overestimates the value of $\Delta H_{desolv}^{phenol+slab}$ for both functionals and cavitation models. For the preferred model (rVV10 with soft sphere), this leads to a misleading agreement with the high coverage experimental value of $\Delta H_{ads,desolv}$ (-35.51 kJmol^{-1} vs. -21.0 kJ mol^{-1}), where one would expect a significantly more negative enthalpy in accordance with observations of phenol under low coverage. The likely source of this error is the oversolvation of the Pt(111) surface, leading to a compartively large value of $\Delta H_{\mathrm{desolv}}^{\mathrm{phenol+slab}}$. The overestimated solvation energy for the Pt surface is moderately reduced when one considers that the implicit solvent solvates a smaller surface area than the explicit solvent (corresponding to 7.5 Pt atoms in the soft sphere model as opposed to 9 Pt atoms for the phenol footprint in the explicit model), which still results in a discrepancy of approximately 40 kJ mol^{-1} for ΔH_{desolv}^{slab}. Conversely, the use of the solvation free energy as opposed to the heat of solvation reduces the solvation estimate of phenol compared to the bond additivity analysis (16 kJ mol^{-1} vs. 25 kJ mol^{-1} for $\Delta H_{desolv}^{phenol}$). Error cancellation between $\Delta H_{desolv}^{phenol}$ and ΔH_{desolv}^{slab} reduces the error between the bond additivity analysis and the rVV10 soft sphere model for $\Delta H_{desolv}^{phenol+slab}$ to approximately 30 kJ mol^{-1}. In order

to realize closer agreement with experimental enthalpy values, further parametrization of the Pt cavity must be performed to align the values of $\Delta H_{desolv}^{phenol+slab}$. This emphasizes a need within the catalysis community to find accurate values of free energy changes for transition metal surfaces. Values of the work function change will also need to be taken into consideration, as we anticipate that parametrizing to achieve more accurate solvation enthalpies will lead to deviations from the ideal value of $\Delta\phi_{pol}$ obtained in Section 3.6. However, the scheme shown here provides an outline as to how the implicit solvent model with the soft sphere cavitation method can be used to obtain qualitative agreement with experimental enthalpy changes under aqueous conditions.

3.5 Electronic Structure of the Metal/Solvent Interface

The newly parametrized soft sphere cavity captures the overall charge displacement induced by explicit water, which gives quantitatively accurate work function values. However, this does not guarantee physical changes in the electronic structure take place. Figure 4 shows the density difference profiles $\Delta\rho(\mathbf{z})$ averaged across the 90 selected snapshots for both the implicit and explicit solvent models. Overall, implicit solvent replicates the electron displacement of the explicit model, with depletion of electron density from the diffuse region and an accumulation at the metallic surface. This corresponds to the 'pillow effect' model of charge displacement, where the electron density of the surficial metal atoms is repelled away from the adsorbate through a Pauli repulsion mechanism.

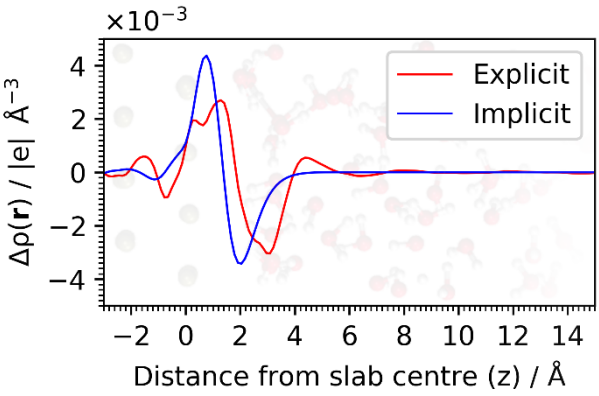

Figure 4: Density difference profile, $\Delta\rho(\mathbf{z})$, averaged across the 90 snapshots for both the explicit and implicit solvent, with z = 0 taken as the first Pt layer.

However, the implicit model does not completely capture certain electronic features of the explicit molecular approach. Most notably, the absence of explicit water shifts the peak appearing at ~ 3 Å to 2 Å and removes its double peak character. This likely arises due to the absence of electron density from the H_2O bi-layer, meaning there is a smaller quantity of charge that can be displaced from the interface region. Furthermore, the implicit solvent method fails to capture the charge accumulation/depletion region in the subsurface region (-2 Å to 0 Å), while also removing the double-peak character of the electron density change.

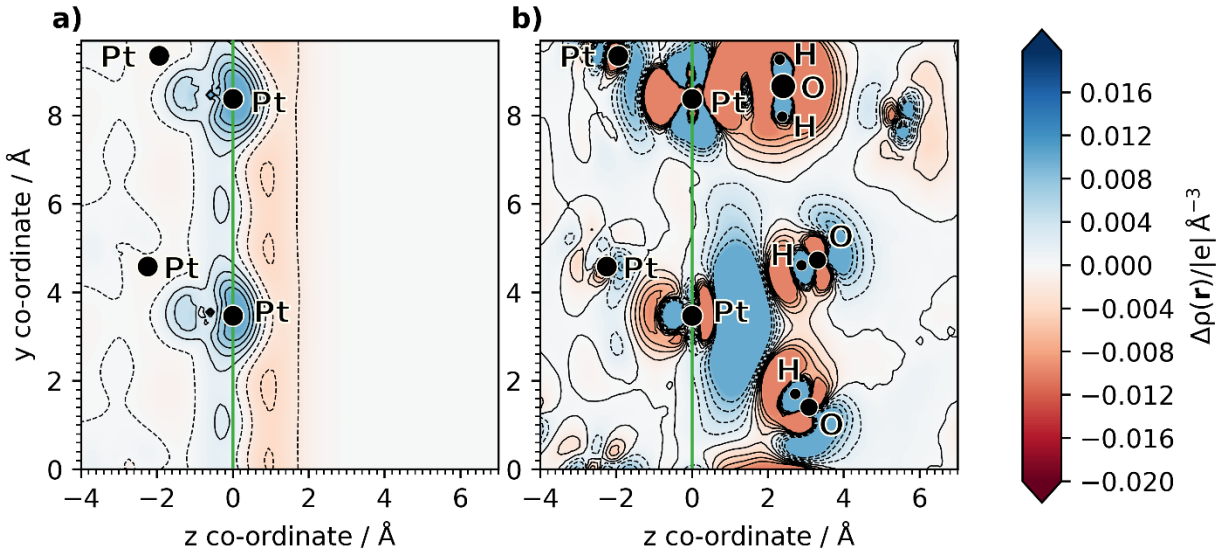

Figure 5: Charge density difference, $\Delta\rho(\mathbf{r})$ across the yz-plane at x = 4.86 Å, for a selected snapshot of: a) the bare slab with implicit solvent and b) the slab with the explicit solvent system. In these models, the first Pt layer is taken as z = 0. Red and blue regions correspond to electron depletion/accumulation respectively. The green line represents the [111] plane at the solvent interface.

Further differences are evidenced in Figure 5, which shows a yz-plane of the Pt/water interface. In the explicit interface, two dominant bonding modes of water feature in the selected plane[72]: H-up ($y \approx 8.5$ Å) where bonding takes place through the oxygen lone-pair and; H-down ($y \approx 4.6$ & 1.3 Å), where water and Pt form a 3-centre bond. In both bonding modes, chemisorption induces significant and complex pattern of charge re-arrangement. The H-up arrangement results in a displacement of charge from the interface due to Pauli repulsion between the oxygen lone pair and the metallic electron density.[72] Conversely, the H-down configuration results in charge accumulation between water and Pt, which contrasts which the Pauli repulsion model of the Pt/H_2O interface. Previous AIMD simulations show that the H-up configuration at the Pt(111) surface dominates,[28] which justifies the negative value of $\Delta\phi_{pol}$.

In contrast, the implicit solvent approach displaces electronic density through a simple charge polarization mechanism. This results in homogenous charge displacement towards the surface, with no re-hybridization of the surface states taking place due to the absence of bonding interactions. These two modes of charge re-arrangement lead to dissimilar electronic structure changes for the surface states of Pt. This is evidenced by the density of states (DOS) plot of Figure 6, which shows the projected d-states of the first layer of Pt atoms for both solvent models, as well as their DOS differences compared to the Pt slab in vacuum. Both solvent models produce a similar degree of distortion, but these induced changes are inconsistent across the d-band. This

is most prominent between -4 and -2 eV, where the molecular water induces an increase in the DOS at the -3.4 eV peak and a slight depletion of the -2.6 eV peak, whereas the continuum model reverses this observation. In addition, the implicit interface exhibits larger changes in d-states close to the Fermi level, especially for the trough at -1 eV, whereas the explicit interface has more pronounced distortions in the more negative regions of the d-band. Furthermore, as discussed by Le et al.,[19] interaction with the Pt surface leads to significant broadening of the band states of water, while the valence band penetrating the Fermi level of Pt is evidence of charge transfer across the surface/solvent interface. Considering both this and the charge density difference of Figure 5, we conclude that the charge re-arrangement at the interface arises through differing mechanisms for implicit and explicit solvent.

However, despite these differences in the electronic structure, the implicit solvent model replicates the overall displacement of charge towards the metallic surface that we observe with the explicit solvent model, correctly replicating electrochemical properties. This highlights the potential of the continuum solvent approach for further study in both catalytic and electrochemical studies.

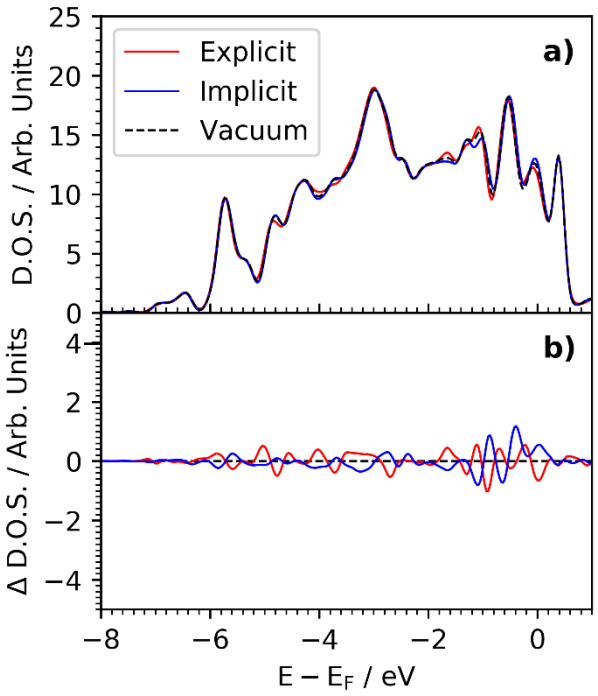

Figure 6: a) Projected Density of States (PDOS) of the surface Pt atoms, projected into the d-band, averaged across 90 AIMD snapshots for the explicit Pt(4x4x4)/H_2O interface, vacuum Pt(4x4x4) and Pt(4x4x4)/continuum interface with the soft sphere model. Energies relative to the Fermi level, E_F. b) Difference of the PDOS d-band with respect to the Pt surface in vacuum.

4 Conclusions

In this study, we performed a comparison of the Poisson-Boltzmann continuum solvent model and explicit solvent AIMD approaches for the Pt(111)/water interface in terms of their description of the electrochemical interface.

We demonstrated a solute cavity parametrization method for the implicit solvent model to obtain equilibrium solvent work function changes due to the electronic structure changes of the AIMD simulations. Central to this method is the assumption that the work function change arises mainly

through electron re-arrangement at the Pt/H_2O interface ($\Delta\phi_{pol}$ = -1.2 eV), while the net dipole of water at the interface makes a relatively small contribution ($\Delta\phi_{orient}$ = +0.3 eV). We also remarked on the use of dispersion including functionals in relation to the work function, where use of the rVV10 functional resulted in systematically higher values (0.2 eV), bringing computed values closer to experimental values in vacuum compared to non-dispersion including GGA functionals.

We further compared the ability of soft sphere and isodensity cavitation approaches to obtain accurate solvation enthalpies for the phenol/Pt(111) adsorption process. As the soft sphere model can parametrize the dielectric cavities of organic and metallic species separately, one can capture the solvation energetics of phenol and the metallic surface, as well as the work function of Pt in solvent. As a result, it was possible to corroborate the observations of bond additivity approaches, which predict that the introduction of solvent does not significantly alter the adsorption energy of phenol under low coverage.

Additionally, we showed that the implicit solvent model was able to reproduce the Pauli repulsion induced push-back of the explicit Pt/H_2O interface. However, the projected DOS of the Pt surface showed the continuum model produced dissimilar d-band distortions compared to molecular H_2O. This was a consequence of the various modes of water binding to the surface Pt, where overlap between the valence states of water and the d-band result in charge transfer as well as van der Waals' repulsion. Contrastingly, the continuum solvent resulted in a simpler homogenous pushback of charge towards the surface, resulting in less pronounced changes across the d-band, but producing larger changes closer to the Fermi level.

The work outlines a technique to obtain equilibrium properties of the electrochemical interface using a computationally inexpensive continuum solvent model that retains the salient electronic structure features of an explicit model. We also showed the importance of separately parametrizing

the dielectric cavity for lighter elements and the heavier metallic atoms. We further note that this scheme does not apply to surfaces which introduce a significant degree of orientational order to the explicit water layer, as the implicit solvent cannot represent the intrinsic dipole of atomistic water. Further developments could use this parametrization approach to construct a more general scheme for a range of metallic surfaces, which will allow computationally efficient simulations of interfacial processes for applications in areas such as electrocatalysis, energy storage and materials science.

Corresponding Author

* vanda.glezakou@pnnl.gov (V.-A. G.); roger.rousseau@pnnl.gov (R. R.);

C.Skylaris@soton.ac.uk (C.-K. S.)

Author Contributions

The manuscript was written through contributions of all authors. All authors have given approval to the final version of the manuscript.

ACKNOWLEDGMENT

G.B. (partial support), V.-A.G., M.-T.N. and R.R. were supported by the U.S. Department of Energy (DOE), Office of Science, Office of Basic Energy Sciences, Division of Chemistry, Geochemistry and Biological Sciences, and located at Pacific Northwest National Laboratory (PNNL). Computational resources were provided by National Energy Research Scientific Computing Center (NERSC), a DOE Office of Science User Facility located at Lawrence Berkeley National Laboratory (LBNL). PNNL is operated by Battelle for the US Department of Energy under Contract DE-AC05-76RL01830. Computational resources were provided by PNNL

Research Computing and the National Energy Research Scientific Computing Center (NERSC), a DOE Office of Science User Facility supported by the Office of Science of the U.S. DOE, located at Lawrence Berkeley national lab (LBNL). G.B. acknowledges the EPSRC for partial support in PhD funding. The authors acknowledge the use of the IRIDIS High Performance Computing Facility (IRIDIS 5), and associated support services at the University of Southampton in the completion of this work. We are grateful to the UK Materials and Molecular Modelling Hub (Thomas HPC) for computational resources, which is partially funded by EPSRC (EP/P020194/1).

Supporting Information

Benchmarking the properties for the Pt bulk (bulk modulus and lattice constant) and Pt(111) surface (surface energy, work function and interlayer relaxation) in vacuum, with respect to k-point spacing and the number of layers; comparison of the topology and DoS between soft sphere and isodensity dielectric cavities for the Pt(111) surface; Distribution of water for the Pt(111)/water interface in the AIMD simulation; Description of the water rotation dynamics using a autocorrelation function; Analysis of the water exchange rate at the Pt(111)/water interface; Calculation of the estimated value of ΔH_{solv} for a single Pt atom using bond additivity analysis; List of all enthalpy changes used in Scheme 1 and the proportions of the Pt(6x6) surface covered by the phenol cavity.

5 References

1. Furimsky, E., Catalytic hydrodeoxygenation. *Appl. Catal. A-Gen.* **2000,** *199*, 147-190.
2. Huber, G. W.; Iborra, S.; Corma, A., Synthesis of Transportation Fuels from Biomass: Chemistry, Catalysts, and Engineering. *Chem. Rev.* **2006,** *106*, 4044-4098.
3. Eslamibidgoli, M. J.; Huang, J.; Kadyk, T.; Malek, A.; Eikerling, M., How theory and simulation can drive fuel cell electrocatalysis. *Nano Energy* **2016,** *29*, 334-361.
4. Nørskov, J. K.; Abild-Pedersen, F.; Studt, F.; Bligaard, T., Density functional theory in surface chemistry and catalysis. *Proc. Natl. Acad. Sci.* **2011,** *108*, 937.

5. Singh, N.; Sanyal, U.; Fulton, J. L.; Gutiérrez, O. Y.; Lercher, J. A.; Campbell, C. T., Quantifying Adsorption of Organic Molecules on Platinum in Aqueous Phase by Hydrogen Site Blocking and in Situ X-ray Absorption Spectroscopy. *ACS Catal.* **2019,** *9*, 6869-6881.
6. Yang, G. J.; Akhade, S. A.; Chen, X.; Liu, Y.; Lee, M. S.; Glezakou, V. A.; Rousseau, R.; Lercher, J. A., The Nature of Hydrogen Adsorption on Platinum in the Aqueous Phase. *Angew. Chem. Int. Ed.* **2019,** *58*, 3527-3532.
7. Michel, C.; Zaffran, J.; Ruppert, A. M.; Matras-Michalska, J.; Jedrzejczyk, M.; Grams, J.; Sautet, P., Role of water in metal catalyst performance for ketone hydrogenation: a joint experimental and theoretical study on levulinic acid conversion into gamma-valerolactone. *Chem. Commun.* **2014,** *50*, 12450-12453.
8. Qiao, Y. Y.; Xu, F. F.; Xu, S. L.; Yang, D.; Wang, B.; Ming, X.; Hao, J. H.; Tian, Y. Y., Pyrolysis Characteristics and Kinetics of Typical Municipal Solid Waste Components and Their Mixture: Analytical TG-FTIR Study. *Energy & Fuels* **2018,** *32*, 10801-10812.
9. Varghese, J. J.; Mushrif, S. H., Origins of complex solvent effects on chemical reactivity and computational tools to investigate them: a review. *React. Chem. Eng.* **2019,** *4*, 165-206.
10. Shang, C.; Liu, Z. P., Origin and Activity of Gold Nanoparticles as Aerobic Oxidation Catalysts in Aqueous Solution. *J. Am. Chem. Soc.* **2011,** *133*, 9938-9947.
11. Cuesta, A., Measurement of the surface charge density of CO-saturated Pt(111) electrodes as a function of potential: the potential of zero charge of Pt(111). *Surf. Sci.* **2004,** *572*, 11-22.
12. Yoon, Y.; Rousseau, R.; Weber, R. S.; Mei, D. H.; Lercher, J. A., First-Principles Study of Phenol Hydrogenation on Pt and Ni Catalysts in Aqueous Phase. *J. Am. Chem. Soc.* **2014,** *136*, 10287-10298.
13. Kim, J.; Kim, H.; Lee, W.-J.; Ruqia, B.; Baik, H.; Oh, H.-S.; Paek, S.-M.; Lim, H.-K.; Choi, C. H.; Choi, S.-I., Theoretical and Experimental Understanding of Hydrogen Evolution Reaction Kinetics in Alkaline Electrolytes with Pt-Based Core–Shell Nanocrystals. *J. Am. Chem. Soc.* **2019,** *141*, 18256-18263.
14. Tripkovic, V.; Bjorketun, M. E.; Skulason, E.; Rossmeisl, J., Standard Hydrogen Electrode and Potential of Zero Charge in Density Functional Calculations. *Phys. Rev. B* **2011,** *84*, 11.
15. Trasatti, S., The Absolute Electrode Potential - an Explanatory Note (Recommendations 1986). *Pure Appl. Chem.* **1986,** *58*, 955-966.
16. Rousseau, R.; De Renzi, V.; Mazzarello, R.; Marchetto, D.; Biagi, R.; Scandolo, S.; del Pennino, U., Interfacial electrostatics of self-assembled monolayers of alkane thiolates on Au(111): Work function modification and molecular level alignments. *J. Phys. Chem. B* **2006,** *110*, 10862-10872.
17. Sakong, S.; Gross, A., The Electric Double Layer at Metal-Water Interfaces Revisited Based on a Charge Polarization Scheme. *J. Chem. Phys.* **2018,** *149*, 084705.
18. Sakong, S.; Forster-Tonigold, K.; Gross, A., The Structure of Water at a Pt(111) Electrode and the Potential of Zero Charge Studied from First Principles. *J. Chem. Phys.* **2016,** *144*, 194701.
19. Le, J. B.; Iannuzzi, M.; Cuesta, A.; Cheng, J., Determining Potentials of Zero Charge of Metal Electrodes versus the Standard Hydrogen Electrode from Density-Functional-Theory-Based Molecular Dynamics. *Phys. Rev. Lett.* **2017,** *119*, 016801.

20. Faheem, M.; Saleheen, M.; Lu, J.; Heyden, A., Ethylene glycol reforming on Pt(111): first-principles microkinetic modeling in vapor and aqueous phases. *Catal. Sci.* **2016,** *6*, 8242-8256.
21. Gillan, M. J.; Alfè, D.; Michaelides, A., Perspective: How good is DFT for water? *J. Chem. Phys.* **2016,** *144*, 130901.
22. Jinnouchi, R.; Anderson, A. B., Electronic structure calculations of liquid-solid interfaces: Combination of density functional theory and modified Poisson-Boltzmann theory. *Phys. Rev. B* **2008,** *77*.
23. Sundararaman, R.; Schwarz, K., Evaluating Continuum Solvation Models for the Electrode-electrolyte Interface: Challenges and Strategies for Improvement. *J. Chem. Phys.* **2017,** *146*, 084111.
24. Hörmann, N. G.; Andreussi, O.; Marzari, N., Grand canonical simulations of electrochemical interfaces in implicit solvation models. *J. Chem. Phys.* **2019,** *150*, 041730.
25. Blumenthal, L.; Kahk, J. M.; Sundararaman, R.; Tangney, P.; Lischner, J., Energy level alignment at semiconductor–water interfaces from atomistic and continuum solvation models. *RSC Adv.* **2017,** *7*, 43660-43670.
26. Hörmann, N. G.; Guo, Z.; Ambrosio, F.; Andreussi, O.; Pasquarello, A.; Marzari, N., Absolute band alignment at semiconductor-water interfaces using explicit and implicit descriptions for liquid water. *Npj Comput. Mater.* **2019,** *5*, 100.
27. Saleheen, M.; Heyden, A., Liquid-Phase Modeling in Heterogeneous Catalysis. *ACS Catal.* **2018,** *8*, 2188-2194.
28. Le, J.; Cuesta, A.; Cheng, J., The structure of metal-water interface at the potential of zero charge from density functional theory-based molecular dynamics. *J. Electroanal. Chem.* **2018,** *819*, 87-94.
29. Vydrov, O. A.; Van Voorhis, T., Nonlocal van der Waals density functional: The simpler the better. *J. Chem. Phys.* **2010,** *133*, 244103.
30. Fisicaro, G.; Genovese, L.; Andreussi, O.; Mandal, S.; Nair, N. N.; Marzari, N.; Goedecker, S., Soft-Sphere Continuum Solvation in Electronic-Structure Calculations. *J. Chem. Thoery Comput.* **2017,** *13*, 3829-3845.
31. Skylaris, C. K.; Haynes, P. D.; Mostofi, A. A.; Payne, M. C., Introducing ONETEP: Linear-scaling Density Functional Simulations on Parallel Computers. *J. Chem. Phys.* **2005,** *122*, 084119.
32. Prodan, E.; Kohn, W., Nearsightedness of electronic matter. *Proc. Natl. Acad. Sci. U.S.A.* **2005,** *102*, 11635-11638.
33. Mermin, N. D., Thermal Properties of Inhomogeneous Electron Gas. *Phys. Rev.* **1965,** *137*, 1441-&.
34. Marzari, N.; Vanderbilt, D.; Payne, M. C., Ensemble Density Functional Theory for Ab Initio Molecular Dynamics of Metals and Finite-temperature Insulators. *Phys. Rev. Lett.* **1997,** *79*, 1337-1340.
35. Ruiz-Serrano, A.; Skylaris, C. K., A Variational Method for Density Functional Theory Calculations on Metallic Systems with Thousands of Atoms. *J. Chem. Phys.* **2013,** *139*, 054107.
36. Miller, D. P.; Hooper, J.; Simpson, S.; Costa, P. S.; Tyminska, N.; McDonnell, S. M.; Bennett, J. A.; Enders, A.; Zurek, E., Electronic Structure of Iron Porphyrin Adsorbed to the Pt(111) Surface. *J. Phys. Chem. C* **2016,** *120*, 29173-29181.
37. Blochl, P. E., Projector Augmented-Wave Method. *Phys. Rev. B* **1994,** *50*, 17953-17979.

38. Garrity, K. F.; Bennett, J. W.; Rabe, K. M.; Vanderbilt, D., Pseudopotentials for high-throughput DFT calculations. *Comp. Mat. Sci.* **2014,** *81*, 446-452.
39. Verga, L. G.; Aarons, J.; Sarwar, M.; Thompsett, D.; Russell, A. E.; Skylaris, C. K., Effect of graphene support on large Pt nanoparticles. *Phys. Chem. Chem. Phys.* **2016,** *18*, 32713-32722.
40. Perdew, J. P.; Burke, K.; Ernzerhof, M., Generalized gradient approximation made simple. *Phys. Rev. Lett.* **1996,** *77*, 3865-3868.
41. Fletcher, R.; Witzgall, C., Practical Methods of Optimization. *Math. Comput.* **1989,** *53*, 768-769.
42. Rozzi, C. A.; Varsano, D.; Marini, A.; Gross, E. K. U.; Rubio, A., Exact Coulomb cutoff technique for supercell calculations. *Phys. Rev. B* **2006,** *73*, 205119.
43. Hine, N. D. M.; Dziedzic, J.; Haynes, P. D.; Skylaris, C.-K., Electrostatic interactions in finite systems treated with periodic boundary conditions: Application to linear-scaling density functional theory. *J. Chem. Phys.* **2011,** *135*, 204103.
44. Sohier, T.; Calandra, M.; Mauri, F., Density functional perturbation theory for gated two-dimensional heterostructures: Theoretical developments and application to flexural phonons in graphene. *Phys. Rev. B* **2017,** *96*, 075448.
45. Wood, B.; Foulkes, W. M. C.; Towler, M. D.; Drummond, N. D., Coulomb finite-size effects in quasi-two-dimensional systems. *J. Phys.: Condens. Matter* **2004,** *16*, 891-902.
46. Hutter, J.; Iannuzzi, M.; Schiffmann, F.; VandeVondele, J., CP2K: atomistic simulations of condensed matter systems. *Wiley Interdscip. Rev. Comput. Mol. Sci.* **2014,** *4*, 15-25.
47. Grimme, S.; Antony, J.; Ehrlich, S.; Krieg, H., A Consistent and Accurate ab initio Parametrization of Density Functional Dispersion Correction (DFT-D) for the 94 Elements H-Pu. *J. Chem. Phys.* **2010,** *132*, 154104.
48. Lippert, G.; Hutter, J.; Parrinello, M., A hybrid Gaussian and plane wave density functional scheme. *Mol. Phys.* **1997,** *92*, 477-487.
49. Bussi, G.; Donadio, D.; Parrinello, M., Canonical Sampling Through Velocity Rescaling. *J. Chem. Phys.* **2007,** *126*, 014101.
50. Schienbein, P.; Marx, D., Liquid–Vapor Phase Diagram of RPBE-D3 Water: Electronic Properties along the Coexistence Curve and in the Supercritical Phase. *J. Phys. Chem. B* **2018,** *122*, 3318-3329.
51. Fattebert, J. L.; Gygi, F., Density functional theory for efficient ab initio molecular dynamics simulations in solution. *J. Comput. Chem.* **2002,** *23*, 662-666.
52. Fattebert, J. L.; Gygi, F., First-principles molecular dynamics simulations in a continuum solvent. *Int. J. Quantum Chem* **2003,** *93*, 139-147.
53. Scherlis, D. A.; Fattebert, J. L.; Gygi, F.; Cococcioni, M.; Marzari, N., A Unified Electrostatic and Cavitation Model for First-principles Molecular Dynamics in Solution. *J. Chem. Phys.* **2006,** *124*, 074103.
54. Womack, J. C.; Anton, L.; Dziedzic, J.; Hasnip, P. J.; Probert, M. I. J.; Skylaris, C. K., DL_MG: A Parallel Multigrid Poisson and Poisson-Boltzmann Solver for Electronic Structure Calculations in Vacuum and Solution. *J. Chem. Thoery Comput.* **2018,** *14*, 1412-1432.
55. Dziedzic, J.; Helal, H. H.; Skylaris, C. K.; Mostofi, A. A.; Payne, M. C., Minimal parameter implicit solvent model for ab initio electronic-structure calculations. *Epl* **2011,** *95*.
56. Alvarez, S., A cartography of the van der Waals territories. *Dalton Trans.* **2013,** *42*, 8617-8636.

57. Marenich, A. V. K., C. P.; Thompson, J. D.; Hawkins, G. D.; Chambers, C. C.; Giesen, D. J.; Winget, P.; Cramer, C. J.; Truhlar, D. G., Minnesota Solvation Database - Version 2012. **2012**.
58. Cheng, J.; Sprik, M., Alignment of electronic energy levels at electrochemical interfaces. *Phys. Chem. Chem. Phys.* **2012,** *14*, 11245-11267.
59. Trasatti, S., Structure of the Metal Electrolyte Solution Interface - New Data for Theory. *Electrochim. Acta* **1991,** *36*, 1657-1658.
60. Cheng, J.; Liu, X. D.; VandeVondele, J.; Sulpizi, M.; Sprik, M., Redox Potentials and Acidity Constants from Density Functional Theory Based Molecular Dynamics. *Acc. Chem. Res.* **2014,** *47*, 3522-3529.
61. Cheng, J.; VandeVondele, J., Calculation of Electrochemical Energy Levels in Water Using the Random Phase Approximation and a Double Hybrid Functional. *Phys. Rev. Lett.* **2016,** *116*, 086402.
62. Cheng, J.; Sulpizi, M.; Sprik, M., Redox potentials and pKa for benzoquinone from density functional theory based molecular dynamics. *J. Chem. Phys.* **2009,** *131*, 154504.
63. Costanzo, F.; Sulpizi, M.; Valle, R. G. D.; Sprik, M., The oxidation of tyrosine and tryptophan studied by a molecular dynamics normal hydrogen electrode. *J. Chem. Phys.* **2011,** *134*, 244508.
64. Gómez, R.; Climent, V.; Feliu, J. M.; Weaver, M. J., Dependence of the Potential of Zero Charge of Stepped Platinum (111) Electrodes on the Oriented Step-Edge Density: Electrochemical Implications and Comparison with Work Function Behavior. *J. Phys. Chem. B* **2000,** *104*, 597-605.
65. Ambrosio, F.; Guo, Z.; Pasquarello, A., Absolute Energy Levels of Liquid Water. *The Journal of Physical Chemistry Letters* **2018,** *9*, 3212-3216.
66. Fawcett, W. R., The Ionic Work Function and its Role in Estimating Absolute Electrode Potentials. *Langmuir* **2008,** *24*, 9868-9875.
67. Dodia, M.; Ohto, T.; Imoto, S.; Nagata, Y., Structure and Dynamics of Water at the Water–Air Interface Using First-Principles Molecular Dynamics Simulations. II. NonLocal vs Empirical van der Waals Corrections. *J. Chem. Thoery Comput.* **2019,** *15*, 3836-3843.
68. Patra, A.; Bates, J. E.; Sun, J.; Perdew, J. P., Properties of Real Metallic Surfaces: Effects of Density Functional Semilocality and van der Waals Nonlocality. *Proc. Natl. Acad. Sci.* **2017,** *114*, 9188.
69. Singh, N.; Campbell, C. T., A Simple Bond-Additivity Model Explains Large Decreases in Heats of Adsorption in Solvents Versus Gas Phase: A Case Study with Phenol on Pt(111) in Water. *ACS Catal.* **2019,** *9*, 8116-8127.
70. Carey, S. J.; Zhao, W.; Mao, Z.; Campbell, C. T., Energetics of Adsorbed Phenol on Ni(111) and Pt(111) by Calorimetry. *J. Phys. Chem. C* **2019,** *123*, 7627-7632.
71. Cantu, D. C.; Wang, Y.-G.; Yoon, Y.; Glezakou, V.-A.; Rousseau, R.; Weber, R. S., Heterogeneous catalysis in complex, condensed reaction media. *Catal. Today* **2017,** *289*, 231-236.
72. Ogasawara, H.; Brena, B.; Nordlund, D.; Nyberg, M.; Pelmenschikov, A.; Pettersson, L. G. M.; Nilsson, A., Structure and Bonding of Water on Pt(111). *Phys. Rev. Lett.* **2002,** *89*, 276102.

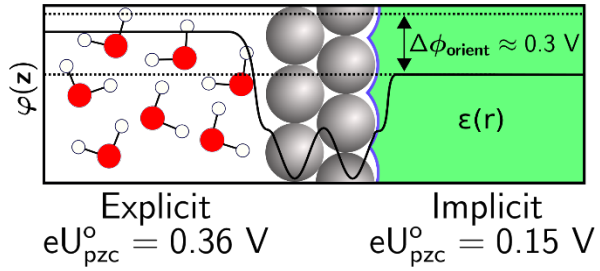

For Table of Contents Only